Scientia Iranica, Vol. 9, No. 2, pp 116–124

SCIENTIA
IRANICA

FEM Simulation of Two- and Three-Electrode Spark Gap Discharges

S. Khorasani[1] and H. Golnabi*

The discharge process in two- and three-electrode pure-nitrogen spark gaps is simulated using Finite Element Method (FEM) to solve for the electric potential and field. The effects of secondary electron emission, photo-ionization and recombination mechanisms are taken into account. Current growth and the evolution of ion and electron distributions in the discharges are studied and an oscillation due to cathode streamer movements has been observed, in agreement with the theoretically estimated values. The study of complete discharges has been possible by introducing proper absorbing boundary conditions over the electrodes, by which numerical instabilities have been suppressed. The simulation results for different values of applied voltage, pressure, gap distance, series resistance and series inductance are discussed. In the case of three-electrode spark gaps, the effect of the trigger voltage on the current buildup speed is considered. Agreement between the calculated closing time for the two-electrode spark gap and a reported empirical formula is observed.

INTRODUCTION

The simulation of avalanche breakdown and ionization growth has been considered in several papers. In earlier works [1], the one-dimensional problem had been solved, with the approximation that the radius of the discharge is much larger than the gap separation. However, this condition is not always met and a more exact formulation appears by assuming a cylindrical charge distribution and applying the disk method to evaluate the electric field [2]. To integrate the charge density variations, the method of characteristics was introduced for low pressures and low overvoltages, and good agreement between theory and experiment was observed. The method was, then, applied in other works [3-5]. Discharges with high pressures and high overvoltages were considered in [6] using the method of characteristics with very short time intervals. An improved one-dimensional simulation has been reported in [7], in which some numerical instabilities associated with the finite difference scheme used had been removed, resulting in a more stable scheme. Due to the significance of the changes in the effective discharge radius, a two-dimensional treatment was presented in [8]. However, the computation was only extended to the end of the first cathode-directed streamer. The early stage of channel formation in a short-gap breakdown was considered in [9] by solving the two-dimensional Poisson equation and conservation equations corresponding to electrons, ions and excited particles. In [10], a kinetic model for the glow phase of an air spark gap was developed in which heavy-particle collision effects are included, and the results were noticed to be in good agreement with the empirical formula presented in [11]. An extensive study of the triggering mechanism in trigatrons was made in [12].

In the two previous works, the structure of a two- [13] and a three-electrode triggerable spark gap with variable gap distance [14] for nitrogen laser drive was described, both operating with pure nitrogen gas. The cross-section diagrams of these spark gaps are presented in Figure 1. In this paper, the discharge behavior in the above spark gaps is simulated to study their performances. In view of the numerical accuracy and stability required for simulations of discharges especially in three-electrode spark gaps, the variational Finite Element Method (FEM) [15,16] was chosen and applied. As will be discussed, proper absorbing boundary conditions have been introduced to permit a continuing simulation after the first cathode-directed streamer, thus extending the simulation to longer times. In the simulation results presented here, a series of oscillations was noticed which was related to

1. *Department of Electrical Engineering, Sharif University of Technology, Tehran, I.R. Iran.*
*. *Corresponding Author, Institute of Water and Energy, Sharif University of Technology, Tehran, I.R. Iran.*

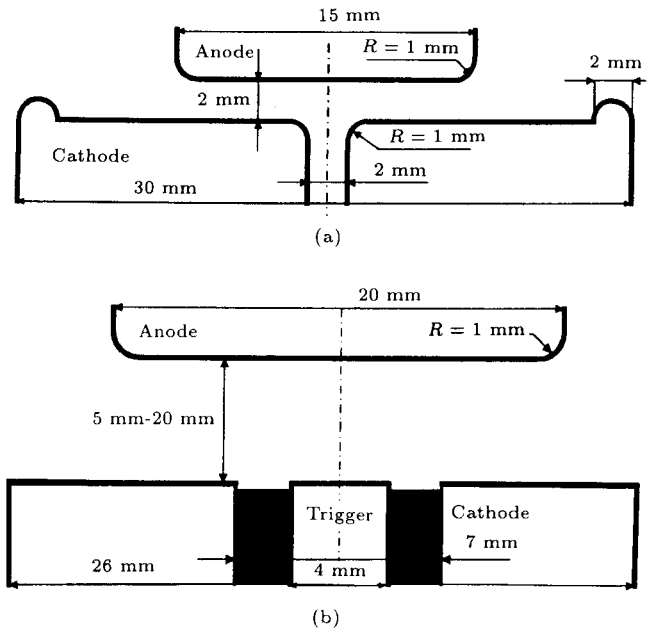

Figure 1. Cross-sections for the two- and three-electrode nitrogen spark gaps [13,14].

the delay in the propagation of electrons across the gap. The observed period shows good agreement with the predicted theoretical values. Also, the effects of series inductance, resistance, gap separation, pressure, applied gap and trigger voltage on the current growth have been studied.

MATHEMATICAL MODEL

To analyze the time evolution of a spark gap discharge, the current growth due to several carrier-generation mechanisms has to be considered. There are three mechanisms contributing appreciably. The first one is ionization by fast electrons moving towards the anode electrode, which results in a nearly exponential increase in the densities of positive and negative carriers, i.e., ions and electrons. This is referred to as the primary ionization and is responsible for avalanche behavior in the breakdown. The second mechanism is the release of secondary electrons from the cathode surface by positive N_2^+ ions falling onto the latter. However, for the atmospheric pressures involved here, the dominant effect is the photo-ionization [17] resulting from the excitation of atoms by the electrons; the transport of radiated photons to the cathode surface and the subsequent release of electrons. It should be noticed that for nitrogen gas, the effect of negative N_2^-ions was negligible due to their instability; also, the primary ionization by ions is small and is ignored throughout this calculation. However, the effect of recombination of electrons and positive ions is significant near or below breakdown and hence is not neglected.

Taking all of the above mechanisms into account, the continuity equations for the two charge species are found as:

$$\frac{\partial \rho_e}{\partial t} = -\alpha(E,p)J_e - \nabla.\mathbf{J_e} - \frac{\rho_e}{\tau} = + \alpha(E,p)\rho_e \mathbf{v}_e - \nabla.(\rho_e \mathbf{v}_e) - \frac{\rho_e}{\tau}, \quad (1a)$$

$$\frac{\partial \rho_i}{\partial t} = +\alpha(E,p)J_e - \nabla.\mathbf{J_i} - \frac{\rho_i}{\tau} = -\alpha(E,p)\rho_e \mathbf{v}_e - \nabla.(\rho_i \mathbf{v}_i) - \frac{\rho_i}{\tau}, \quad (1b)$$

where $\rho_e = \rho_e(\mathbf{r},t) < 0$ and $\rho_i = \rho_i(\mathbf{r},t) > 0$ are the electron and (positive) ion volume charge densities, $\mathbf{r} = r\hat{\mathbf{r}} + z\hat{\mathbf{z}}$ is the position vector and t denotes time, $\mathbf{J_e} = \rho_e \mathbf{v}_e(\mathbf{E},p)$ and $\mathbf{J}_i = \rho_i \mathbf{v}_i(\mathbf{E},p)$ are the electron and ion current densities with $\mathbf{v}_e$ and $\mathbf{v}_i$ the electron and ion drift velocities, respectively. $\alpha(E,p)$ is the first Townsend coefficient, or ionization coefficient, which is equal to the number of ionizing collisions of an electron moving one unit distance, and is expressed as a function of the local electric field strength E and gas pressure p. Also, the del operator, $\nabla = \hat{\mathbf{r}}\partial/\partial r + \hat{\mathbf{z}}\partial/\partial z$, is defined in axisymmetric cylindrical coordinates. Numerical values of $\alpha, \mathbf{v}_e$ and $\mathbf{v}_i$ in terms of the local electric field and pressure for nitrogen gas were obtained from [18], through fitting by some proper functions. τ is the characteristic recombination time of the two charge species and is considered to be independent of the applied voltage [17]. Since at the breakdown voltage, the recombination rate roughly balances the generation rate, an approximation to the recombination time τ can be written as:

$$\tau \approx [\alpha(E_b,p)\mathbf{v}_e(\mathbf{E}_b,p)]^{-1}, \quad (2)$$

where $\mathbf{E}_b$ is the breakdown electric field estimated from an empirical equation for the breakdown voltage V_b [19]:

$$V_b = 6.72\sqrt{pd} + 24.36\ pd. \quad (3)$$

Here, d is the gap separation in cm and V_b and p are given in kilovolts and bars, respectively.

As can be seen from Relations 1, the ionization coefficients and drift velocities are functions of the local electric field $\mathbf{E}$, which is obtainable as the gradient of the potential distribution. For the first stages of breakdown, when the current is in the range of several microamperes, the effect of space charges on the potential field may be neglected, for which Laplace equation provides good results. However, the effect of space charges becomes significant at higher currents. To obtain an accurate solution, it is necessary to solve Poisson equation for the scalar electric potential $\phi = \phi(\mathbf{r},t)$. It is evident that the gap separation is small

enough to neglect the displacement current density, and a scalar potential can be defined as:

$$\nabla^2\phi = -\frac{\rho_e + \rho_i}{\varepsilon}, \tag{4a}$$

$$\mathbf{E} = -\nabla\phi, \tag{4b}$$

in which ε is the permittivity of the nitrogen gas, being approximately equal to the permittivity of free space, ε_0. If the gap length is much smaller than the wavelength of the associated electromagnetic wave determined by the order of the current buildup rate, then the second Kirchohff law for current conservation (KCL) is applicable and the displacement current $\partial\mathbf{D}/\partial t$ can be neglected. Therefore, the magnetostatic approximation of current distribution is valid and the electric potential description of the electric field would be consistent.

Equation 4a is subject to the boundary conditions:

$$\phi(\mathbf{r},t)|_{z=0,r>r_t} = 0$$

on the cathode surface, (5a)

$$\phi(\mathbf{r},t)|_{z=d} = V_g(t)$$

on the anode surface, (5b)

$$\phi(\mathbf{r},t)|_{z=0,r<r_t} = V_t(t)$$

on the trigger surface
(for a triggerable spark gap), (5c)

$$\frac{\partial\phi(\mathbf{r},t)}{\partial_{\mathbf{n}}}|_{r=0,r=r_{\max}} = 0$$

on the axis of the spark gap and the rest of the boundary, (5d)

where $V_g(t)$ and $V_t(t)$ are the time-varying potentials of the anode and the trigger (if any) and r_t is the radius of the trigger. Condition 5d imposes axial symmetry about the $r = 0$ axis and also prevents the current density field lines from leaking out of the system over the boundaries $r = r_{\max}$; thus, the sum of the electrode currents is always zero, as required by Kirchoff second circuit law. Obviously, in practice this condition is not satisfied exactly; however, it is required later for compatibility with the equations for the external circuitry. It also results in a small error in the calculations, since in practice the current density lines are not simply confined to such boundaries.

The set of Equations 1 results in charge accumulation near the electrodes with opposite polarities. To suppress subsequent numerical instabilities, proper absorbing boundary conditions have been introduced as:

$$\frac{\partial\rho_e}{\partial t}|_{z=d} = -\nabla\cdot\mathbf{J}_e + \frac{J_e}{\delta}$$

on the anode surface, (6a)

$$\frac{\partial\rho_i}{\partial t}|_{z=0} = -\nabla\cdot\mathbf{J}_i - \frac{J_i}{\delta} + \frac{\rho_e}{\tau}$$

on the cathode and trigger surface, (6b)

$$\rho_i(\mathbf{r},t)|_{z=d} = 0$$

on the anode surface, (6c)

where δ is the characteristic distance of the absorption rate, here equal to the height of a finite element. The physical interpretation of the absorption terms is simple: On the anode surface, the electrons enter the electrode metal, and on the cathode surface, the ions recombine with the electrons, with a rate proportional to the current density. Equation 6c states that the ion density over the anode is nearly zero. This process is fairly comparable to the current transport in $p-n$ junctions by holes and electrons. If this absorption mechanism is ignored, an artificial charge accumulation over the electrode surface will be developed. These charge layers would produce a very strong reverse electric field which counters the external gap field. Therefore, the current buildup would be stopped and the gap current reduces to zero.

It is possible to express the absorption mechanism by allowing the electrode boundaries to be 'transparent' with regard to the charge species which are traveling towards them. This is implemented numerically through Equations 6a and 6b. In each time step, some of the accumulated charge over the electrode surface should be depleted. A simple picture of this process can be drawn in two ways: either a time constant is associated with the absorption, or the current density decays to zero with a length scale. If the proper time constant is considered, some measurements might be required. However, for this purpose, the second picture is more adequate which is as follows.

The used finite element formulation produces a piecewise linear distribution of the variables. Therefore, the relative charge distribution is dropped to zero in a length equal to or shorter than a finite element length. Numerically, shorter absorption lengths reproduce the same results while larger absorption lengths result in a net extra charge accumulation. This is because shorter absorption lengths cannot be 'sensed' by the finite elements, since the variation of parameters are supposed to be linear. Correspondingly, the selection of a larger length leads to the absorption of charges across two or several finite elements. However,

there is only one single boundary element over the anode or the cathode surface across the gap, so that a net charge accumulation would be observed.

The effects of secondary electrons and photo-ionization have been included in an additional boundary condition for the electron charge density ρ_e over the cathode and trigger surfaces [8]:

$$\rho_e(\mathbf{r},t)|_{z=0} = -\frac{J_0(\mathbf{r},t)}{\mathbf{v}_e(\mathbf{r},t)} - \gamma_i \frac{J_i(\mathbf{r},t)}{\mathbf{v}_e(\mathbf{r},t)} + \frac{\gamma_{ph}}{\mathbf{v}_e(\mathbf{r},t)} \iiint_v \beta(\mathbf{r}',t) g(\mathbf{r},\mathbf{r}') \rho_e(\mathbf{r}',t) dv', \tag{7}$$

where $J_0(\mathbf{r},t)$ is the photo-electric current density [7] and V denotes the axisymmetric integration enclosed volume within the gap. J_0 is an externally triggered current by an ultraviolet flash, initiating the discharge; γ_i and γ_{ph} are the secondary and photo-ionization coefficients, representing the number of electrons released per incident, ion and photon, respectively; $\beta(\mathbf{r}',t)$ is the rate of excitation per electron and $g(\mathbf{r}.\mathbf{r}')$ is the average number of photon incidents on the cathode at $\mathbf{r}$, released per excited atom at $(\mathbf{r}')$ in random direction. Note that in Relation 7 the effect of field emission for the three-electrode gap has been neglected due to the lack of sharp corners in the trigger electrode. Details regarding these functions are presented below.

Numerical values for the photoelectric current density $J_0(\mathbf{r},t)$, the secondary electron emission coefficient γ_i, and the total ionization coefficient $\gamma_T = \gamma_i + \gamma_{ph}$ have been considered using the data given in [8,17,20], respectively. The function $g(\mathbf{r},\mathbf{r}')$ may be simply shown to be [8]:

$$g(\mathbf{r},\mathbf{r}') = \frac{|z-z'|}{4\pi} \int_0^{2\pi} \frac{\exp\left(-|\mathbf{r}-\mathbf{r}'|/\lambda\right) d\theta}{|\mathbf{r}-\mathbf{r}'|^3}, \tag{8}$$

where λ is the mean decay constant of photo-ionization radiation in nitrogen, being about 2.5 cm [17]. The coefficient $\beta(\mathbf{r}',t)$ is roughly approximated as:

$$\beta(\mathbf{r}',t) \approx n \sum_{\sigma}^{N_2} C[E(\mathbf{r}',t),p], \tag{9}$$

where n is the number density of gas molecules and the summation is done for all excitable states σ; ${}^{N_2}_{\sigma}C$ is the excitation rate of the state σ. The values of the excitation rates of the Nitrogen molecule are given in [21,22].

The system of Equations 1 and 4 through 7 needs to be solved simultaneously with the circuit equations. The external-circuit diagram of the three-electrode spark gap is shown in Figure 2 and values for the circuit elements are given in [23]. (The different circuits used in nitrogen laser drives are discussed in [24].) The

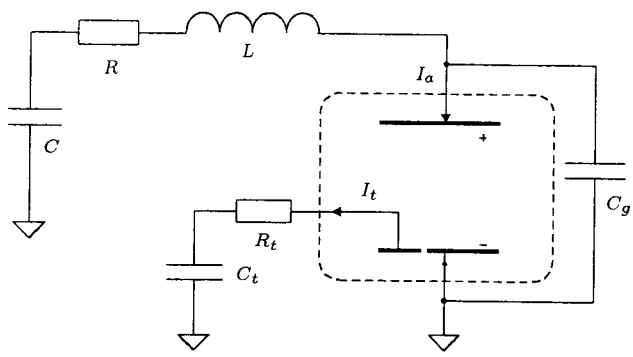

Figure 2. Circuit diagram for the three-electrode spark gap. The equivalent circuit of the two-electrode spark gap is obtained by removing the trigger branch consisting of resistance R_t and capacitance C_t.

state equations [25] for the circuit of the three-electrode spark gap are:

$$\frac{d}{dt}\begin{bmatrix} \nu_g \\ i_L \\ \nu_C \\ \nu_{C_t} \end{bmatrix} = \begin{bmatrix} 0 & C_g^{-1} & 0 & 0 \\ -L^{-1} & -RL^{-1} & L^{-1} & 0 \\ 0 & -C^{-1} & 0 & 0 \\ 0 & 0 & 0 & 0 \end{bmatrix} \begin{bmatrix} \nu_g \\ i_L \\ \nu_C \\ \nu_{C_t} \end{bmatrix} + \begin{bmatrix} -C_g^{-1} I_a(t) \\ 0 \\ 0 \\ C_t^{-1} I_t(t) \end{bmatrix}, \tag{10}$$

where the parameters are illustrated in Figure 2. (The series inductance L consists of the line and channel inductances.) The above system can be used for two-electrode spark gaps if $I_t(t)$ is set identically equal to zero. The electrode currents $I_a(t)$ and $I_t(t)$ can be found from integrating the current densities over the electrode surfaces:

$$I_a(t) = \iint_{\text{anode}} (\mathbf{J}_e + \mathbf{J}_i).d\mathbf{S}, \tag{11a}$$

$$I_t(t) = \iint_{\text{trigger}} (\mathbf{J}_e + \mathbf{J}_i).d\mathbf{S}. \tag{11b}$$

The anode potential $V_g(t)$ is the first component of the state vector and the trigger voltage $V_t(t)$ should be calculated according to:

$$V_t(t) = \nu_{C_t} + R_t I_t(t). \tag{12}$$

Equations 1 and 10 are subject to the initial conditions:

$$\rho_e(\mathbf{r},0) = -\rho_i(\mathbf{r},0) = \rho_0(\mathbf{r}), \tag{13a}$$

$$\begin{bmatrix} \nu_g \\ i_L \\ \nu_C \\ \nu_{C_t} \end{bmatrix}\Bigg|_{t=0} = \begin{bmatrix} V_0 \\ 0 \\ V_0 \\ V_{t_0} \end{bmatrix}, \tag{13b}$$

where $\rho_0(\mathbf{r})$ is the initial charge density produced by an ultraviolet flash which is centralized about the gap axis; V_0 and V_{t_0} are the initial gap and trigger voltages, respectively.

NUMERICAL METHOD

The most important part of the numerical scheme is to calculate the potential distribution in the presence of space charges by solving Poisson Equation 4a subject to the boundary Conditions 5. Because the conditions of continuity and differentiability of the solution are both met by the finite-element method, this method is chosen; in addition, FEM is able to match arbitrary geometries. FEM approaches fall into two categories: Ritz-Galerkin and variational. Here, the variational FEM with first-order elements is employed because it is simple and easy to code. For more discussion on this subject the reader is referred to [15,16].

In the variational FEM, the solution of the differential equation is found by minimizing a functional, namely:

$$\prod(\phi) = \iiint_V \frac{1}{2}|\nabla\phi|^2 - \frac{\rho_e+\rho_i}{\varepsilon}\phi d\nu$$

$$= \iint_\Gamma \left(\frac{1}{2}|\nabla\phi|^2 - \frac{\rho_e+\rho_i}{\varepsilon}\phi\right) 2\pi r\, dr\, dz, \tag{14}$$

where the integration volume V is obtained by revolving the surface Γ around the symmetry axis. To perform the minimization procedure, it is necessary to discretize the solution function by subdividing the integration region Γ into triangular finite elements. Over the boundary and inside each element, the variation of the potential is supposed to be both continuous and linear. The functional (Equation 14) is minimized through setting the partial derivatives with respect to the potential values at the nodes (vertices of the elements) equal to zero. Thus, a simultaneous set of linear equations in terms of the potential values at the nodes is obtained from which the potential distribution is found.

After computing the electric field by taking the potential gradient, the new electron and ion densities at each node are calculated according to Equations 1, 6 and 7. The important issue at this stage is the calculation of the divergence terms, which involves differentiation of the current density vectors $\mathbf{J}_e$ and $\mathbf{J}_i$. To prevent related numerical in stabilities, Green theorem is applied to find the divergences as follows:

$$\iint_{\Sigma S^e} \nabla.\mathbf{J}_{e,i} dS^e = \oint_{\Sigma L^e} (d\mathbf{l}^e \times \mathbf{J}_{e,i})_\theta, \tag{15}$$

in which ΣS^e and ΣL^e, respectively, denote the area and boundary of integration, corresponding to the neighboring elements, i.e., elements involving the corresponding node at which the divergence is to be calculated. Here, only the θ component of Equation 15 is considered, because the cross product of the path differential and the current density vectors lie in θ direction. Also, the closed line integral encircles the node in a counter-clockwise direction. Assuming that the divergence is nearly equal in each of the neighboring elements, transforms Equation 15 into the more easily computed form:

$$\nabla.\mathbf{J}_{e,i} = \frac{1}{\Sigma S^e}\Sigma(\mathbf{L}^e \times \mathbf{J}_{e,i})_\theta. \tag{16}$$

Here, the denominator is equal to the total area of integration on the left hand side of Equation 15 and the summation in the numerator is over the external borders $\mathbf{L}^e$ of the neighboring elements. Knowing the divergence of the current-density vectors, it is possible to calculate the new electron and ion densities via integrating Equations 1 and 6. However, the calculation of electron density over the cathode electrode due to secondary and photo-ionizations (Equation 7) involves a triple integral, one of which results from Equation 8. This integral is non-elementary and is numerically calculated.

After computation of the charge densities, the electrode currents are calculated with the aid of Relation 10. Finally, the circuit equations are solved by integrating the time rate of change of the state vector in Equation 11 and the new voltage for the anode (and trigger) electrode is found. Then, the above calculations are repeated until the simulation of the discharge is completed.

SIMULATION RESULTS

The simulation results for the two-electrode spark gap are demonstrated in Figure 3. As expected from the small gap separation (2 mm) and high overvoltage ($\sum$40%), the discharge develops in a short time (about 20 ns) and the current grows into the ampere range. From this moment on, according to the next figures, the discharge speed becomes dependent on the external circuitry. Therefore, the effective discharge closing time would be about 20 ns. Martin empirical fit for two-electrode spark gaps in [11] predicts a closing time of 11.5 ns. Martin fit is correct within a factor of 2, and the presented simulation is consistent with this. From this moment on, the gap behaves as a nearly constant resistive/inductive element, and the RLC approximation to the discharge circuit would be valid. (A complete circuit analysis of the discharge is found in [23,24].) Near 30 ns the current goes up to about 1 kA and the storage

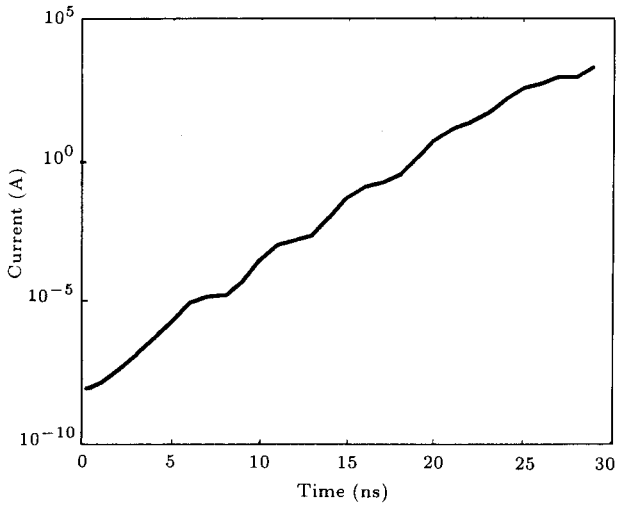

Figure 3. Simulation result for the two-electrode spark gap with $V = 10$ kV, $p = 760$ torr, $R = 0.3\ \Omega, C = 50$ nF and $L = 10$ nH. A current in the ampere range is established after 20 ns.

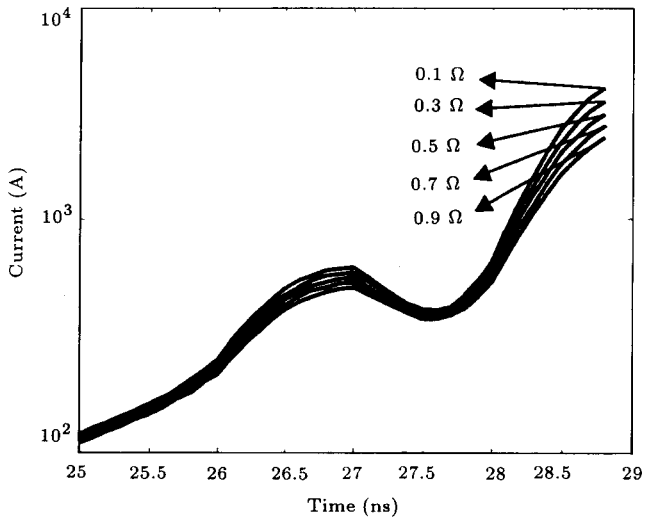

Figure 4. Variation of discharge current as a function of gap resistance, for $R = 0.1, 0.3, 0.5, 0.7$ and $0.9\ \Omega$, respectively, from top to bottom.

capacitor becomes fully discharged; the voltage across the gap drops to zero and the discharge is terminated.

A series of oscillations is observed which are connected with the transit time of electron wavefronts to cross the gap distance. The impact of each electron wavefront on the anode surface produces an oscillation in the total current. Each moving wavefront ionizes the gas molecules and also excites them while broadening the ionized discharge channel. The photons subsequently emitted are transported to the cathode surface and release a new wavefront of electrons, which hits the anode surface after one transit delay time. From Figure 3 the oscillation period may be estimated to be about 4.2 ns, which is close to the theoretically estimated drift time of electrons, about 4.07 ns, derived according to the following formula:

$$T \approx \frac{d}{\mathbf{v}_e(E', p)}, \tag{17}$$

where T is the time delay, d is the gap separation and E' is the corrected electric field which includes the effect of field non-uniformity.

In Figure 4, the current growth for different values of the series resistance between 0.1 Ω to 0.9 Ω is illustrated. When the gap current is under one ampere, the series resistance has no observable effect; indeed, it only limits the peak current and has no influence on the overall discharge speed. This is expected from the small voltage drop across the resistance in the breakdown stages and only a slight difference could be noticed after 25 ns. However, the effect of series inductance is observed as a reduction in the rate of current rise from 22 ns, as illustrated in Figure 5 for inductance values of 0 nH to 40 nH. It is evident

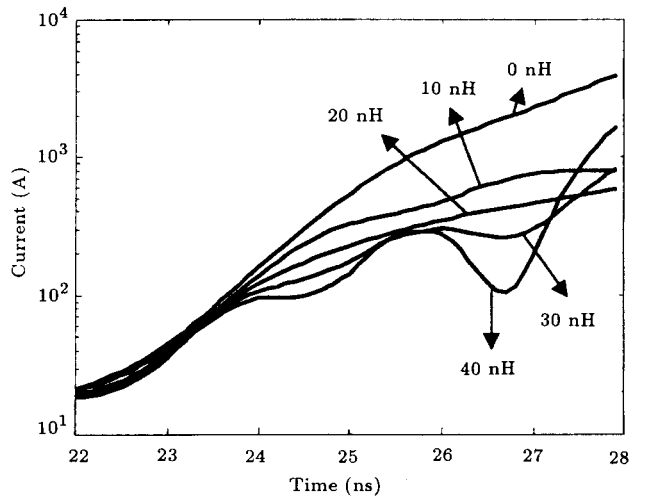

Figure 5. Variation of discharge current as a function of inductance, for $L = 0, 10, 20, 30$ and 40 nH. A difference as high as one order of magnitude in current may be noticed.

that the current is about one order of magnitude higher than when the series inductance is zero. The pressure and voltage effects are rather noticeable as in Figures 6 and 7, because they are directly related to the primary ionization factor $\alpha(E, p)$. This factor is mainly a function of the ratio E/p and drops for field to pressure ratios above a certain value. Here, it is seen that for pressures below 700 torr and gap voltages above 10 kV, the discharge growth speed is lower and approximately the same, respectively. Therefore, the optimal E/p would be about 65 V/cm.torr. Also, for high pressures ($>$ 1000 torr) or low voltages ($<$ 5 kV) no breakdown results, while for voltages higher than 12 kV the growth rate does not change significantly. This is due to the fact that excitation

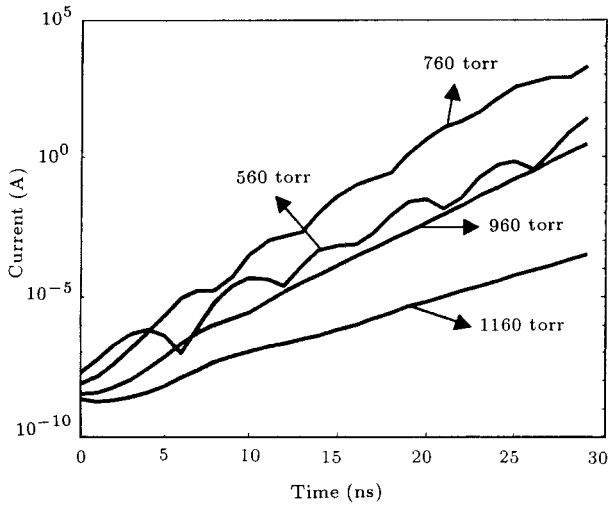

Figure 6. Variation of discharge current as a function of pressure, for $p = 560, 760, 960$ and 1160 torr. There is no breakdown for $p = 1160$ torr.

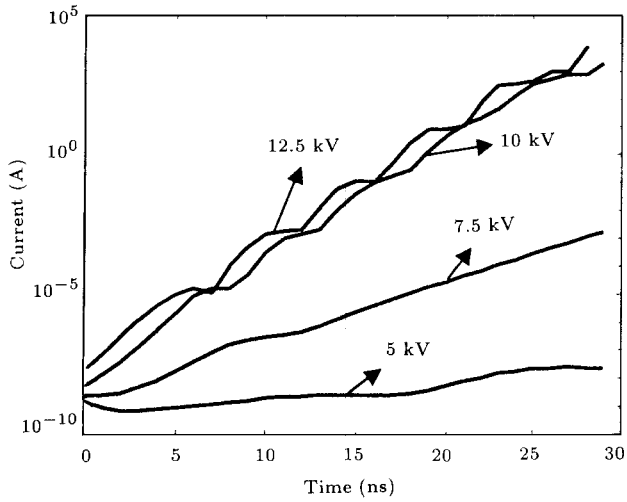

Figure 7. Variation of discharge current as a function of applied voltage, for $V = 5$, 7.5, 10 and 12.5 kV. There is no breakdown for $V = 5$ kV.

and ionization rates have decreased at such pressures or voltages.

A simulation of the discharge current in the three-electrode spark gap is illustrated in Figure 8 with an applied trigger voltage of 5 kV. Because of the larger gap distance (10 mm) and smaller overvoltage (~0.1%), breakdown is much slower and current in the ampere range is established in about 1 μs. The effects of gap voltage, pressure, series resistance and inductance on the current buildup stage are similar to those for the two-electrode gap, and thus are not discussed. Instead, the effect of gap-distance variations is demonstrated in Figure 9. Keeping the other conditions constant, for gap-distances larger than 10 mm breakdown does not occurs and the current decays to zero. The most interesting difference could be observed for different trigger voltages as shown in Figure 10. The higher

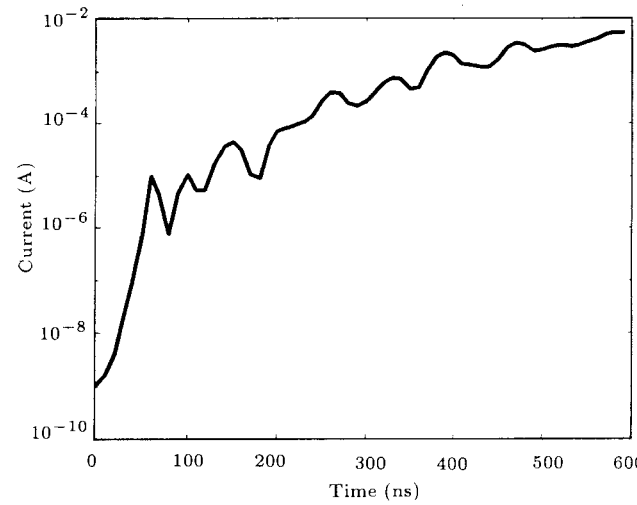

Figure 8. Simulation result for the three-electrode spark gap with $V = 30$ kV, $p = 760$ torr, $R = 0.3\ \Omega$, $C = 50$ nF, $L = 10$ nH and $V_t = 5$ kV, $C_t = 5$ nF, $R_t = 0.03\ \Omega$. A current in the ampere range is established in about 1μs.

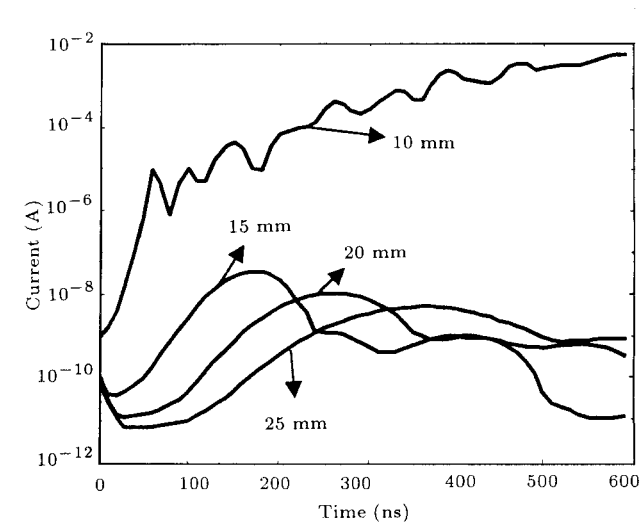

Figure 9. Variation of discharge current as a function of gap separation, for $d = 10, 15, 20$ and 25 mm. There is no breakdown for gap separation larger than 10 mm with $V = 30$ kV, $p = 760$ torr and $V_t = 5$ kV.

the trigger voltage, the higher the speed of current buildup. At the trigger voltage of 10 kV, a strong discharge is observed; after 250 ns, the current value grows up to eight orders of magnitude higher than when no trigger voltage had been applied (i.e., if a two-electrode gap with the same parameters had been used.)

CONCLUSIONS

In this paper, a mathematical model for the simulation of discharges in previously reported two- and three-electrode nitrogen spark gap switches has been described. The effects of primary ionization, secondary electron emission by ions and photons and recombi-

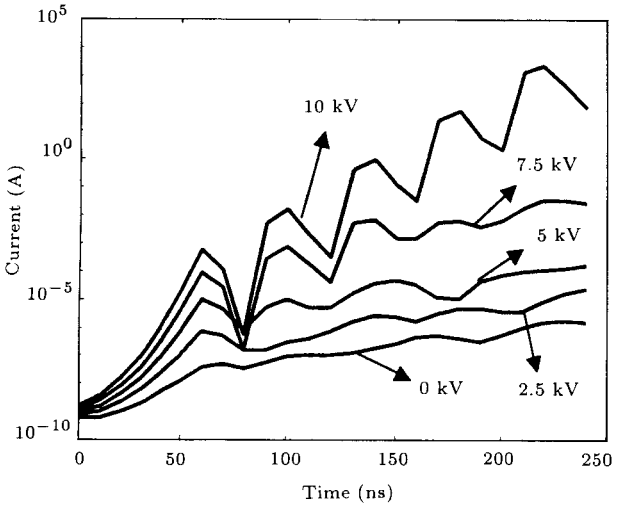

Figure 10. Variation of discharge current as a function of trigger voltage, for $V_t = 0, 2.5, 5, 7.5$ and 10 kV. For a trigger voltage of 10 kV, the current establishes values up to eight orders of magnitude higher than the equivalent two-electrode spark gap with no trigger voltage.

nation have been included. Proper absorbing boundary conditions have been defined to prevent artificial charge accumulation near electrodes and subsequent numerical instabilities. The potential distribution is calculated with the aid of the axisymmetric variational finite element method. The current growth is calculated and a series of oscillations has been noticed. These oscillations have been related to the transit time of electrons across the gap and a good agreement with theoretical estimates, based on this assumption, has been found. The rise times to currents in the ampere range for the reported two- and three-electrode gaps have been estimated. The dependence of current growth on pressure, gap voltage, series inductance and resistance and gap separation has been demonstrated and discussed. It has been noticed that the series inductance could severely limit the current buildup rate.

ACKNOWLEDGMENT

The authors wish to thank the Micro-Technology and Integrated Photonics Laboratories of Electrical Engineering Department, Sharif University of Technology, for providing computational hardware facilities.

REFERENCES

1. Koppitz, J. "Nitrogen discharges of large cross section at high overvoltages in a homogeneous field", *J. Phys. D: Appl. Phys.*, **6**(12), pp 1494-1502 (1973).

2. Reininghaus, W. "Calculation of streamers in gaseous discharges", *J. Phys. D: Appl. Phys.*, **6**(12), pp 1486-1493 (1973).

3. Davies, A.J. and Evans, C.J. "The computation of the growth of a gaseous discharge in space-charge distorted fields", *Comput. Phys. Commum.*, **3**, pp 322-333 (1972).

4. Bayle, P. and Bayle, M. "Simulation of secondary processes in breakdown in air", *Z. Phys.*, **266**, pp 275-281 (1974).

5. Kline, L.E. "Calculation of discharge initiation in overvolted parallel-plane gaps", *J. Appl. Phys.*, **45**, pp 2046-2054 (1974).

6. Davies, A.J., Davies, C.S. and Evans, C.J."Computer simulation of rapidly developing gaseous discharges", *Proc. IEE*, **118**(6), pp 816-823 (1971).

7. Davies, A.J., Evans, C.J. and Woodison, P.M. "Computation of ionization growth at high current densities", *Proc. IEE*, **122**(7), pp 765-768 (1975).

8. Davies, A.J., Evans, C.J., Townsend, P. and Woodison, P.M. "Computation of axial and radial development of discharges between plane parallel electrodes", *Proc. IEE*, **124**(2), pp 179-182 (1977).

9. Novak, J.P. and Bartnikas, R. "Early stages of channel formation in a short-gap breakdown", *J. Appl. Phys.*, **64**(4), pp 1767-1774 (1988).

10. Rodrigues, A.E., Morgan, W.L., Touryan, K.J., Moeny, W.M. and Martin, T.H. "An air breakdown kinetic model", *J. Appl. Phys.*, **70**(4), pp 2015-2022 (1991).

11. Martin, T.H., in Digest of Technical Papers, *7th IEEE Pulsed Power Conference*, Monterey, CA (unpublished), pp 73-79 (1989).

12. Williams, P.F. and Peterkin, F.E. "Triggering in trigatron spark gaps: A fundamental study", *J. Appl. Phys.*, **66**(9), pp 4163-4175 (1989).

13. Golnabi, H. "Reliable spark gap switch for laser triggering", *Rev. Sci. Instrum.*, **63**(12), pp 5804-5805 (1992).

14. Golnabi, H. and Samimi, H. "Triggerable spark gap switches for pulsed gas lasers", *Rev. Sci. Instrum.*, **65**(9), pp 3030-3031 (1994).

15. Zienkiewicz, O.C. and Taylor, R.L., *The Finite Element Method*, 4th Ed., McGraw-Hill, London, **1** (1989).

16. Sadiku, M.N.O., *Numerical Techniques in Electromagnetics*, CRC Press, Reading (1992).

17. Meek, J.M. and Craggs, J.D., Eds., *Electrical Breakdown of Gases*, John Wiley & Sons, Chichester, p 278 (1978).

18. Frommhold, L. "Eine Untersuchung der Elektronenkomponente von Elektronen-lawinen im homogenen Feld II", *Z. Phys.*, **160**, pp 554-567 (1960).

19. Golnabi, H. "Study of breakdown voltages for triggered spark gap switches", *Int. J. Eng.*, **9**(3), pp 143-150 (1996).

20. Doran, A.A. "The development of a Townsend discharge in N_2 up to breakdown investigated by image converter, intensifier and photomultiplier techniques", *Z. Phys.*, **208**, pp 427-440 (1968).

21. Huxley, L.G.H. and Crompton, R.W., *The Diffusion and Drift of Electrons in Gases*, Wiley, New York (1974).

22. Louriero, J. and Ferreira, C.M. "Electron excitation rates and transport parameters in direct-current N_2 discharges", *J. Appl. Phys. D*, **22**, pp 67-75 (1989).

23. Golnabi, H. and Ashrafi, A. "Theoretical studies of electrical characteristics of the nitrogen laser", *Int. J. Eng.*, **7**(3), pp 143-153 (1994).

24. Golnabi, H. "Nitrogen laser charging process investigation", *IEEE J. Quantum Electron.*, **QE-29**, pp 1192-1198 (1993).

25. Desoer, C.A. and Kuh, E.S., *Basic Circuit Theory*, McGraw-Hill, New York, Chap. 12 (1969).